

# UC Berkeley

## UC Berkeley Previously Published Works

### Title

Constraining and Characterizing the Size of Atmospheric Rivers: A Perspective Independent From the Detection Algorithm

### Permalink

<https://escholarship.org/uc/item/0cj3c03f>

### Journal

Journal of Geophysical Research: Atmospheres, 126(16)

### ISSN

2169-897X

### Authors

Inda-Díaz, HA  
O'Brien, TA  
Zhou, Y  
[et al.](#)

### Publication Date

2021-08-27

### DOI

10.1029/2020jd033746

Peer reviewed

# JGR Atmospheres

## RESEARCH ARTICLE

10.1029/2020JD033746

### Special Section:

Atmospheric Rivers: Intersection of Weather and Climate

### Key Points:

- Multiple independent estimates show atmospheric rivers areas are between  $7 \times 10^{11}$  and  $10^{13}$  m<sup>2</sup>, with lower sizes range than ARTMIP estimates
- Landfalling atmospheric rivers from the northwest Pacific are larger and more zonally oriented than those from the northeast Pacific
- In general, atmospheric rivers tend to decrease their size and become more meridionally oriented through their life cycles

### Supporting Information:

Supporting Information may be found in the online version of this article.

### Correspondence to:

T. A. O'Brien,  
obrienta@iu.edu

### Citation:

Inda-Díaz, H. A., O'Brien, T. A., Zhou, Y., & Collins, W. D. (2021). Constraining and characterizing the size of atmospheric rivers: A perspective independent from the detection algorithm. *Journal of Geophysical Research: Atmospheres*, 126, e2020JD033746. <https://doi.org/10.1029/2020JD033746>

Received 24 AUG 2020

Accepted 23 JUN 2021

### Author Contributions:

**Conceptualization:** H. A. Inda-Díaz, T. A. O'Brien, W. D. Collins

**Formal analysis:** H. A. Inda-Díaz, T. A. O'Brien, W. D. Collins

© 2021. Lawrence Berkeley National Laboratory.

This is an open access article under the terms of the [Creative Commons Attribution-NonCommercial-NoDerivs License](#), which permits use and distribution in any medium, provided the original work is properly cited, the use is non-commercial and no modifications or adaptations are made.

# Constraining and Characterizing the Size of Atmospheric Rivers: A Perspective Independent From the Detection Algorithm

H. A. Inda-Díaz<sup>1,2</sup> , T. A. O'Brien<sup>1,3</sup> , Y. Zhou<sup>1</sup> , and W. D. Collins<sup>1,4</sup> 

<sup>1</sup>Lawrence Berkeley National Laboratory, Berkeley, CA, USA, <sup>2</sup>University of California Davis, Davis, CA, USA, <sup>3</sup>Indiana University Bloomington, Bloomington, IN, USA, <sup>4</sup>University of California Berkeley, Berkeley, CA, USA

**Abstract** Atmospheric rivers (AR) are large and narrow filaments of poleward horizontal water vapor transport. Because of its direct relationship with horizontal vapor transport, extreme precipitation, and overall AR impacts over land, the AR size is an important characteristic that needs to be better understood. Current AR detection and tracking algorithms have resulted in large uncertainty in estimating AR sizes, with areas varying over several orders of magnitude among different detection methods. We develop and implement five independent size estimation methods to characterize the size of ARs that make landfall over the west coast of North America in the 1980–2017 period and reduce the range of size estimation from ARTMIP. ARs that originate in the Northwest Pacific (WP) (100°–180°E) have larger sizes and are more zonally oriented than those from the Northeast Pacific (EP) (180°–240°E). ARs become smaller through their life cycle, mainly due to reductions in their width. They also become more meridionally oriented toward the end of their life cycle. Overall, the size estimation methods proposed in this study provide a range of AR areas (between  $7 \times 10^{11}$  and  $10^{13}$  m<sup>2</sup>), that is, several orders of magnitude narrower than current methods estimation. This methodology can provide statistical constraints in size and geometry for the AR detection and tracking algorithms, and an objective insight for future studies about AR size changes under different climate scenarios.

**Plain Language Summary** Atmospheric rivers (AR) are a meteorological phenomenon with strong poleward water vapor transport. ARs have positive and negative impacts over the regions where they make landfall, particularly for West Coast US water resources. AR size (length, width, and area) is an important characteristic that needs to be studied, and could directly relate to the impacts of AR over land. There are large differences in size estimation between current detection methods, with areas varying over several orders of magnitude. Our study focuses on characterizing AR size using five different methods independent of the AR detection algorithm. We find that North American landfalling ARs originated in the North Pacific have areas between  $7 \times 10^{11}$  and  $10^{13}$  m<sup>2</sup> (between 1 and 11 times the area of California), and their lengths are on average four times their widths. ARs originating from the Northwest Pacific (WP) (100°–180°E) are bigger and more parallel to the equator than those from the Northeast Pacific (EP) (180°–240°E). Our methods provide a narrower range of size estimation than the current methods and could be used to constrain current and future AR detection methods, and it could be used in future studies to understand how AR size could vary under climate change scenarios.

## 1. Introduction

Atmospheric rivers (ARs) are long and narrow filaments of poleward water vapor transport from the tropics (Newell et al., 1992; Ralph et al., 2018; Zhu & Newell, 1998), that carry over 90% of the meridional moisture transport from the tropics to higher latitudes but may occupy only about 10% of the total longitudinal length (Zhu & Newell, 1998). Midlatitude continental regions around the world have large amounts of precipitation associated with ARs (Lavers & Villarini, 2013b; Neiman et al., 2008; Ramos et al., 2015; Viale et al., 2018; Waliser & Guan, 2017). ARs are associated with up to half of the extreme events in the top 2% of the precipitation and wind distribution across most midlatitude regions (Waliser & Guan, 2017). Moreover, landfalling ARs are associated with about 40%–75% of extreme wind and precipitation events over 40% of the world's coastlines (Waliser & Guan, 2017). ARs can have both positive and negative effects in continental regions. Their absence can lead to droughts (Dettinger, 2013), whereas numerous ARs can

**Investigation:** H. A. Inda-Díaz, T. A. O'Brien  
**Methodology:** H. A. Inda-Díaz, T. A. O'Brien, Y. Zhou  
**Project Administration:** T. A. O'Brien, W. D. Collins  
**Software:** H. A. Inda-Díaz, T. A. O'Brien, Y. Zhou  
**Supervision:** T. A. O'Brien  
**Writing – original draft:** H. A. Inda-Díaz  
**Writing – review & editing:** H. A. Inda-Díaz, T. A. O'Brien, Y. Zhou, W. D. Collins

lead to flooding and other hydrological hazards (Dettinger, 2011; Lavers & Villarini, 2013a; Ralph & Dettinger, 2011; Ralph et al., 2006). Ultimately, ARs have important consequences in the hydrological cycle of regions like California. They contribute to the accumulation of the snowpack and the reservoir level and water availability (Dirmeyer & Brubaker, 2007; Eldardiry et al., 2019; Goldenson et al., 2018; Guan et al., 2010; Kim et al., 2013).

Along with horizontal vapor transport, AR size (length and width) is an important characteristic that needs to be better understood. Nevertheless, a robust connection between AR size and their impacts over land and intensity scale still has to be studied and determined. Ralph et al. (2019) introduced a scale to categorize AR strength based on vapor transport intensity and landfall duration and show that there are beneficial and hazardous impacts associated with AR events. If ergodicity relates AR size and duration, AR size could be directly related to the benefits and hazards associated with them. Therefore, in addition to integrated vapor transport (IVT) and AR duration, the question “how large are atmospheric rivers?” represents a key aspect of research in the AR research community.

The Atmospheric River Tracking Method Intercomparison Project (ARTMIP) has made an international effort to understand whether and how our scientific understanding of ARs may depend on the detection algorithm. The different ARTMIP detection and tracking algorithms are designed to answer different questions, and they produce differences in AR climatology (Lora et al., 2020; Rutz et al., 2019; Shields et al., 2018); therefore, there are differences in their detected shape and size. It has become clear that AR detection and tracking are heavily influenced by how researchers have quantitatively defined this phenomenon, for example, the use of  $250 \text{ kg m}^{-1} \text{ s}^{-1}$  minimum threshold for IVT, which does not account for size but only for the concentration of flow and moisture levels. These different rules and algorithm thresholds have resulted in large uncertainty in estimating the AR size, with areas varying over several orders of magnitude among different detection methods (see Figure 1).

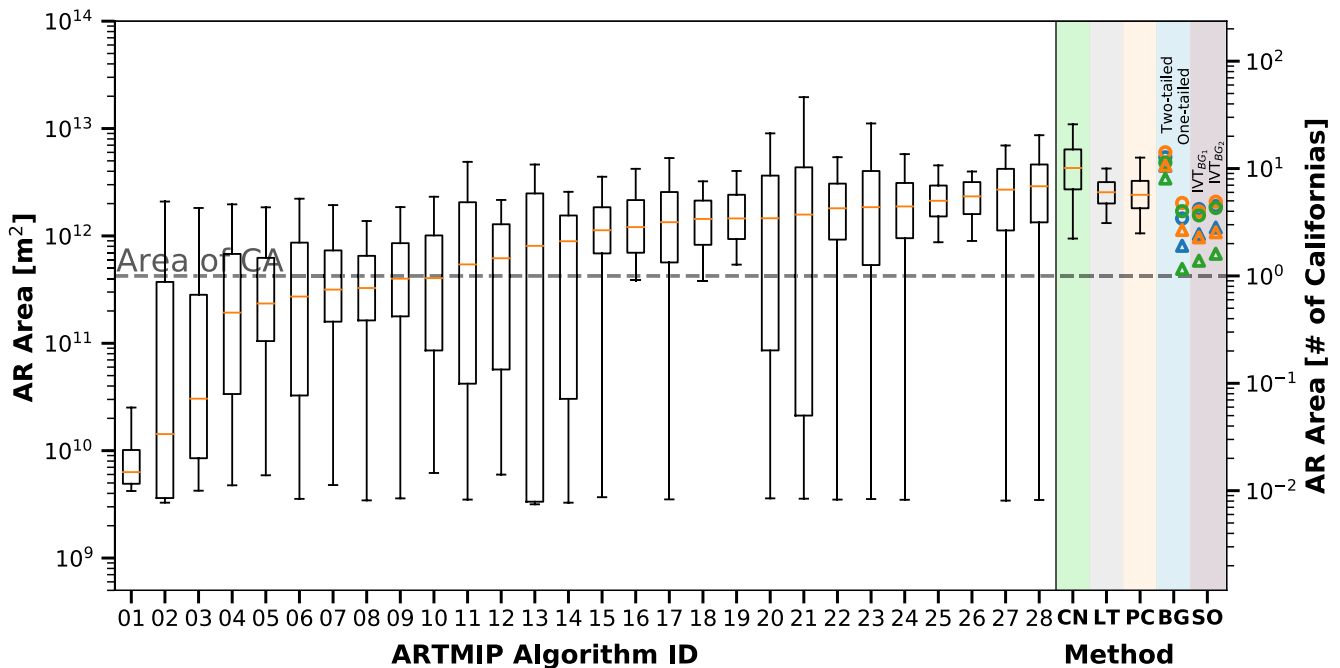


**Figure 1.** White background: AR area calculated from different methods in ARTMIP, ordered by median area (01–28). Colored background: AR area calculated in this study using the ClimateNet ARTMIP campaign (CN), Lagrangian Tracers method (LT), Principal Component Analysis of IVT (PC), KS-test between the IVT of AR and the background IVT field (BG), and the statistical overlapping of the conditional probability distribution of IVT given distance to the center of AR and the background IVT probability density function (SO): see Sections 3.1–3.4 for details. For BG and SO methods, triangles represent the composite of AR with Northeast Pacific origin (EP) and circles represent the composite of AR with Northwest Pacific origin (WP). Blue, orange, and green markers account for 25%, 50%, and 75% of the AR life cycle, respectively. For the BG method, we show the results from the two-tailed and one-tailed KS-test. For the SO method, we show the results using  $IVT_{BG1}$  and  $IVT_{BG2}$ , that correspond to a  $p \geq \sigma^+$  at  $179.5$  and  $193.9 \text{ kg m}^{-1} \text{ s}^{-1}$ , respectively. (Algorithm names are included in Table S1 for reference).

The definition of the boundaries and size quantification of ARs are ongoing research questions, and therefore a great uncertainty among methods is expected. Some recommendations made after the formal AR definition in the Glossary of Meteorology in 2018 were “to keep the definition as short as possible and to leave specifications of how the boundaries of an AR are to be quantified open for future and specialized developments” (Ralph et al., 2018).

The research described in this manuscript works toward the development and implementation of five independent AR size estimation methods. Since we do not develop a new AR detection algorithm, and the methods described here are not directly related to any existing AR detection or tracking algorithm, we argue that they collectively provide a robust and objective way to estimate AR size with a lower range of AR sizes than ARTMIP. The methods presented in this study do not preclude the possibility that the parameter choices are made by the same group of people. Nevertheless, we used statistical quantities to estimate ARs size and objectively tested these methods' sensitivity to the chosen parameters. For this study, we analyze the winter (November–April) North American coast landfalling ARs and create a composite for the 1980–2018 period, to objectively estimate the size of ARs using the IVT from ERA5 reanalysis data (European Centre for Medium-Range Weather Forecasts, 2019).

## 2. Data

In this study, we use the AR detection results from three different ARTMIP methods (Rutz et al., 2019; Shields et al., 2018): CASCADE\_BARD\_v1 (O'Brien et al., 2020), Lora\_global (Lora et al., 2017), and Mundhenk\_v3 (Mundhenk et al., 2016). Employing these three different detection algorithms allows us to broadly sample ARs in the North Pacific Ocean. Each of these methods generates a binary flag: 1 for “AR conditions exist” and 0 for “AR conditions do not exist”; for each latitude-longitude grid point. AR binary flags were calculated using thermodynamic and dynamical fields from the Modern-Era Retrospective Analysis for Research and Applications Version 2 (MERRA-2) reanalysis (Gelaro et al., 2017) as a part of the ARTMIP Tier 1 experiment (Shields et al., 2018). In the methods section, we describe how we use these binary flags to create the AR composite.

The column-integrated water vapor (IWV) and IVT, are the two main variables used to define and characterize ARs (Ralph et al., 2018). For this study, we focus on IVT and calculate it using the vertically integrated eastward and northward water vapor flux [ $\dot{q}_x, \dot{q}_y$ ] ( $\text{kg m}^{-1} \text{s}^{-1}$ ) provided by the ERA5 reanalysis. IVT is defined as

$$\text{IVT} = \sqrt{\dot{q}_x^2 + \dot{q}_y^2}, \quad (1)$$

where

$$\dot{q}_x = -\frac{1}{g} \int_{p_b}^{p_t} q u dp, \quad (2)$$

$$\dot{q}_y = -\frac{1}{g} \int_{p_b}^{p_t} q v dp, \quad (3)$$

$q$  is the specific humidity [ $\text{kg kg}^{-1}$ ],  $u$  and  $v$  are the zonal and meridional wind velocity [ $\text{m s}^{-1}$ ] over the pressure surface  $p$ ,  $P_b$  is 1,000 hPa,  $P_t$  is 200 hPa, and  $g$  is the gravitational acceleration. We also use  $u$  and  $v$  for the Lagrangian in Section 3.3. ERA5 data have a temporal resolution of 1 h and a horizontal resolution of  $0.25^\circ$ . We focus our study on the 1980–2017 period.

Following O'Brien et al. (2020), to avoid the large contiguous regions of high IVT near the tropics associated with the intertropical convergence zone (ITCZ), we spatially filter the IVT field as

$$IVT' = IVT \cdot \left( 1 - e^{\frac{-y^2}{2\Delta y^2}} \right), \quad (4)$$

where  $IVT'(x, y)$  is the filtered IVT field,  $x$  and  $y$  are the longitude and latitude, respectively, and  $\Delta y$  is half-width at half-maximum of the filter. We use  $\Delta y = 15^\circ$ , which effectively damps the IVT to zero within the ITCZ. Hereon, we refer to the filtered field as IVT for simplicity.

This analysis focuses on 37 wet seasons (November–April) in the 1980–2017 period over the North American coast. We focus on landfalling ARs and effectively restrain the study domain to the North Pacific Basin ( $0^\circ$ – $90^\circ$ N,  $100^\circ$ – $240^\circ$ E).

Furthermore, since this study's primary focus is to study the size of ARs, we only utilize output from the three ARTMIP algorithms to obtain a broad and robust sample of AR occurrences (time and approximate location). With the exception of the areas shown in Figure 1, we explicitly avoid using the exact shape or size determined by any detection and tracking algorithm.

### 3. Methods

We apply the AR life cycle tracking algorithm from Zhou et al. (2018) to the AR binary flag data (from the three detection methods used in this study) and record each detected AR position and timestamp. To ensure we sample over the highest possible number of ARs and avoid double-sampling events, we start by taking all the ARs detected from one tracking method. We add the AR events from the second tracking method that are not detected by the first, and finally, we add the ones from the third method that are not in the first or the second. It is essential to note that we only record the AR time stamp and center coordinates of each object through its life cycle (calculated using Equations 7 and 8), and we do not infer the shape or size of ARs from these detection algorithms. Our size-estimating methods later use the recorded AR center as a first guess on the time and location of an AR.

In this fashion, we create a 1980–2017 wet season (November–April) data set of North American coast landfalling AR objects. Each object corresponds to one instantaneous snapshot of an AR and contains its center's timestamp and location through its life cycle. The data set is divided into two parts, based on AR origin location (Northwest Pacific “WP”  $100^\circ$ – $180^\circ$ E vs. Northeast Pacific “EP”  $180^\circ$ – $240^\circ$ E); and classified by its life cycle stage, at 25%, 50%, and 75% of the AR total life cycle. All subsequent analyses and methods in this study are applied separately for each of these six sub-data sets.

#### 3.1. Principal Component Analysis of IVT (PC Method)

Recognizing that ARs are associated with ridge-like structures in the IVT field, the principal components (PCs) method is designed to estimate AR size by modeling AR shapes as Gaussian. For each object, we apply principal component analysis (PCA) to the high IVT cluster closest to the AR object's center (or first guess) and compute the weighted covariance matrix  $C_w$  (Price, 1972) of latitude and longitude

$$C_w = \frac{\sum_{i=1}^{n_x} \sum_{j=1}^{n_y} IVT_{ij} (x_{ij} - \bar{x})^T (y_{ij} - \bar{y})}{\sum_{i=1}^{n_x} \sum_{j=1}^{n_y} IVT_{ij}}, \quad (5)$$

where  $x_{ij}$  and  $y_{ij}$  are the longitude and latitude of the ERA5 grid,  $\bar{x}, \bar{y}$  are the spatial zonal and meridional mean, and the weight is given by the  $IVT_{ij}$  at each grid point.  $C_w$  is a  $2 \times 2$  matrix, such that

$$C_w \begin{pmatrix} \bar{s}_0 \\ \bar{s}_1 \end{pmatrix} = \begin{pmatrix} \lambda_0 \bar{s}_0 \\ \lambda_1 \bar{s}_1 \end{pmatrix}, \quad (6)$$

where the eigenvectors  $\bar{s}_0, \bar{s}_1$  are the principal components of the IVT field, and  $\lambda_0, \lambda_1$  are the eigenvalues. The principal components represent the directions of maximum variance of the IVT field near the AR. The

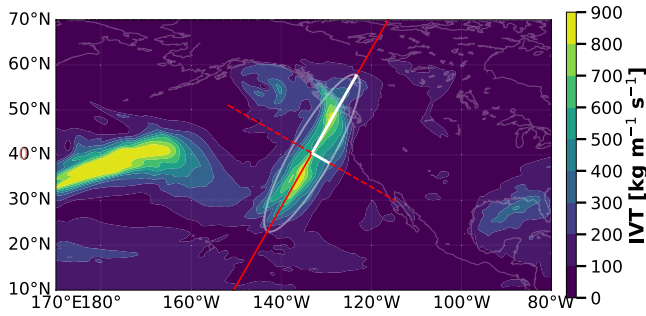


**Figure 2.** Principal component analysis method. White lines represent the PC of the atmospheric river (AR), and the white contour is the area estimated from the ellipse whose axes are the PC. The red lines represent directions along and across AR used to sample integrated vapor transport for SO and BG methods (dashed/solid represent the first/second PC).

largest eigenvalue represents the direction that explains the largest IVT variance, hence the longest AR axis (along the AR,  $\bar{s}_0$ ), while the smallest would represent the shortest AR axis (across the AR,  $\bar{s}_1$ ).

To filter the IVT field, that is, far from one AR object, we use a two-step iterative method. First, we find the IVT cluster closest to the first guess location and define the AR “core” as the point where IVT is greater than 0.5 times the local maximum IVT. We apply PCA to the AR core and use the eigenvalues and eigenvectors to create a 2D Gaussian function using Equation 11. Then, we filter all the points from the original ERA5 IVT field where the core Gaussian function is less than  $10^{-3}$  (we found this value worked well for the ARs objects analyzed in this study). We then apply PCA to the filtered IVT field and use the results to estimate the size of the AR object.

We define the length (width) of the AR as two times the magnitude of  $\bar{s}_0$  ( $\bar{s}_1$ ), and its area as the ellipse whose axes are the principal components  $\bar{s}_0$  and  $\bar{s}_1$  (white solid lines and ellipse in Figure 2). The AR orientation  $\theta$  is

defined as the angle between  $\bar{s}_1$  and the equator. Estimating the area of an AR as an ellipse is an idealization that allows us to simplify the problem and avoid the introduction of more rules and thresholds that would essentially result in a new detection algorithm. We realize that this will affect the calculation of areas with more highly irregular AR shapes. However, in a case-by-case inspection, we find that this is a good approximation for the average AR in this study. Moreover, an overlap plot of all the AR events (Figure 8) shows that, on average, this is an adequate idealized model representation of ARs, which becomes particularly relevant for the statistical methods described in Section 3.2. We utilize fastKDE (O’Brien et al., 2014, 2016) to calculate probability density functions (PDFs) of length, width, area, and orientation, using all the AR objects in our six sub-data sets (<https://github.com/LBL-EESA/fastkde/releases/tag/v1.0.18>). The method described in this section—applying PCA to the IVT field and define length and width—is labeled PC throughout this study.

### 3.2. Estimating AR Size From Composites and Background IVT Field (BG and SO Methods)

To estimate the AR length and width, we use two different statistical methods for determining the distance at which the AR composite becomes indistinguishable from the background IVT field (from now on referred only as background for simplicity). We create an AR composite from a total of 1,150 (980) AR objects for the WP (EP) in the 1980–2017 wet seasons. We randomly sub-sample 300 AR objects (from each region) to ensure independence between each AR object used to create the composite and increase the statistical robustness of these methods.

The statistical overlapping method (SO) looks at the overlapping between the background PDF and the composite as a function of the distance to the AR center. On the other hand, the background method (BG) uses a Kolmogorov-Smirnov test (KS-test) to look at the difference between the background cumulative distribution function (CDF) and the conditional probability distribution (CPD) of the composite IVT given the distance to the AR center. We describe both methods in Sections 3.2.2 and 3.2.3. For the SO and BG methods, we calculate the AR composite area by modeling the shape of ARs as ellipses, whose axes are the length and width calculated by each method.

We define the AR center coordinates  $(\bar{x}, \bar{y})$  for every AR object within the composite as the IVT-weighted center of mass:

$$\bar{x} = \frac{\sum_{i=1}^{n_x} \sum_{j=1}^{n_y} \text{IVT}_{ij} x_{ij}}{\sum_{i=1}^{n_x} \sum_{j=1}^{n_y} \text{IVT}_{ij}}, \quad (7)$$



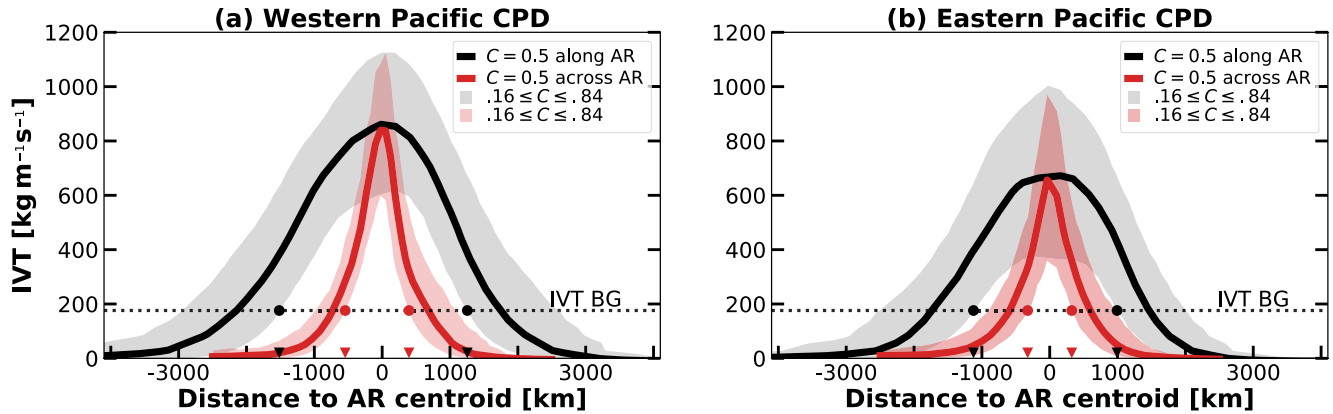


**Figure 3.** Conditional probability distribution of integrated vapor transport (IVT) given the distance to the center of the atmospheric river (AR). Red colors represent the transverse direction (across AR), black colors represent the longitudinal direction (along AR). The 0.5 conditional probability  $C$  is represented in solid thick lines. The shading corresponds to probabilities between 0.16 and 0.84. According to the statistical overlapping method, the AR is delimited by those distances where the dashed line (background  $IVT \geq 0.84$ ) intersects the 0.16 CPD contour (marked in red and black dots). For example, for the Northwest Pacific composite (WP) in panel (a), these intersections occur at approximately from  $-1,500$  to  $1,200$  km along the AR, and  $-600$  and  $400$  km across the AR. The triangles mark these distances of overlapping with the background.

$$\bar{y} = \frac{\sum_{i=1}^{n_x} \sum_{j=1}^{n_y} IVT_{ij} y_{ij}}{\sum_{i=1}^{n_x} \sum_{j=1}^{n_y} IVT_{ij}} \quad (8)$$

We then sample IVT along the direction of the principal components (see Section 3.1) through all the domain (represented by the red lines in Figure 2), and calculate the distance  $d$  of each point along this line to the AR center

$$d = \| (x', y') - (\bar{x}, \bar{y}) \|, \quad (9)$$

where  $(x', y')$  represent the coordinates of the points along each of the principal components' direction. In this fashion, we create a joint distribution of IVT and  $d$  for the AR composite, and utilize fastKDE to calculate the CPD of IVT given  $d$ :  $P(IVT | d)$ .

### 3.2.1. Estimation of the Background

We estimate the PDF and CDF of the background by randomly sampling IVT from ERA5 reanalysis data through the North Pacific Ocean in the period of study. Since the definition of “background” is somewhat ambiguous, we calculate two separate backgrounds:  $IVT_{bk_1}$ , where the grid cells inside an AR are masked at the time of sampling (AR grid cells not used to calculate the background); and  $IVT_{bk_2}$ , where ARs are not masked at the time of IVT sampling. Despite the fact that  $IVT_{bk_2}$  includes high-IVT points inside some ARs, we remark that both backgrounds are statistically indistinguishable with a confidence level of 95% according to a two-sample KS-test. The CDF of the background is higher than 0.84 ( $p \geq \sigma^+$ , where  $\sigma^+$  is the value of CDF at +1 standard deviation) at  $179.5$  and  $193.9$   $\text{kg m}^{-1} \text{s}^{-1}$  for  $IVT_{bk_1}$  and  $IVT_{bk_2}$  respectively, which are later used for the SO and BG methods (Sections 3.2.2 and 3.2.3) and referred to in the text label in Figure 1.

### 3.2.2. Statistical Overlapping of IVT With the Background Field PDF (SO)

One way to estimate the AR composite's length and width is by looking at the overlap of the background PDF and the composite IVT conditional probability distribution given the distance to the center of AR (CPD( $d$ )). We define the statistical boundary of the AR composite as the distance where the CPD( $d$ ) = 0.16 contour is greater or equal to the background IVT value at CDF = 0.16. In other words, where CPD( $d$ ) at  $-1$  standard deviation ( $\sigma^1$ ) intersects with the background PDF at +1 standard deviation ( $\sigma^+$ ) (where the lower boundary of the shading contour intersects the dotted line in Figure 3). With this method, we determine the AR extent by determining the distance  $d$  where the overlap between the composite PDF and the background PDF is less than two standard deviations. This method is referred to as SO throughout this study.

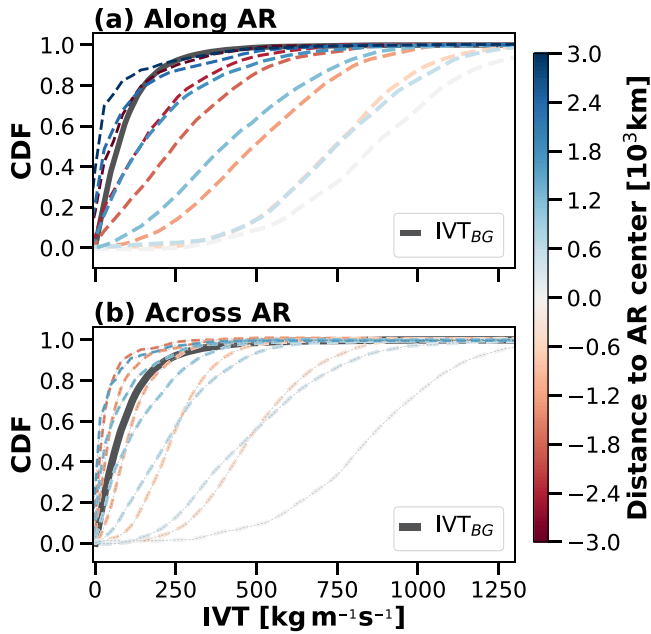


**Figure 4.** Colored lines show the CDF of IVT for the AR composite, at different distances from the AR center (CDF(d)); less transparent dashed lines represent a farther distance to the AR center. The black solid line shows the CDF of the background. The KS-test evaluates where the composite IVT and the background are statistically indistinguishable (for the two-tailed test) or where the composite IVT CDF is statistically lower than the background CDF (for the one-tailed test).

### 3.2.3. K-S Statistics Between AR Composite and the Background CDF (BG)

The KS-test is used to determine at which distance the CDF of the composite IVT is indistinguishable from the background CDF. This method assumes that the IVT distribution within ARs differs from the background.

From the CPD(d), we calculate the CDF of the composite IVT at different distances along and across the AR composite (CDF(d)). We compare the CDF(d) against the background CDF (4) and apply two-tailed and one-tailed KS-tests (KS1 and KS2, respectively). For the KS1, we define the AR boundaries at the distance where the background CDF is significantly lower than the background at the 95% confidence level. For the KS2, the AR boundaries are delimited by those distances at which the KS-statistic reaches a minimum value, that is, where the CDF(d) and the background CDF are most similar. Figure 4 shows how the CDF(d) (colored dashed lines) converges to the background CDF (solid black line) far from the center of the AR composite ( $d = 0$  km, represented by the most transparent dashed lines).

Both BG and SO methods provide a robust statistical estimation of the AR composite size. In the supporting information, we show a test of the sensitivity of the SO method to changes in the background PDF and to changes in the CPD(d) overlapping values; we also test the sensitivity of the BG method to changes in the statistical level of significance for the one-tailed BG method (Text S1 and Figures S1a and S1b).

### 3.3. Lagrangian Tracers for Area Estimation (LT)

Previous study by Garaboa-Paz et al. (2015) suggests that ARs relate to attracting Lagrangian Coherent Structures (LCS) in the 2D and 3D flow fields. With this in mind, we hypothesize that Lagrangian tracers can be used to estimate AR area from a fluid dynamics point of view. The association of ARs with LCS implies that tracers inside the AR are more likely to preserve spatial coherence through backward and forward trajectory integration. Furthermore, tracers near the boundaries and outside of the AR, compared with those inside the AR, would be more likely to disperse and end up at a final location farther from its initial location.

To do so, we use a 2D passive Lagrangian tracer advection model. Tracers are advected over pressure surfaces using 2D velocity fields from ERA5 reanalysis following a stochastic advection equation

$$dx_i = (u_i + \sqrt{2}\bar{u}_i w_i)dt, \quad (10)$$

where  $i$  represents the zonal or meridional directions,  $u$  the 2D velocity over pressure surfaces,  $\bar{u}_i$  is the root mean square of the local velocity near the tracer (Griffa et al., 1995; LaCasce, 2008; Rodean, 1996; Sawford, 1991), and  $w_i$  is a random perturbation with zero mean and unit variance (i.e., a Wiener process). This random nudging in the tracer position at each step helps represent diffusion, turbulence, and other processes not resolved by the model. In Text S2 and Figure S2, we show a test of the sensitivity of AR area to changes of the scaling velocity  $\sqrt{2}\bar{u}_i$ . We solve Equation 10 using the Euler method with a time-step of 1 h (same as the ERA5 resolution, thus avoiding the need for time interpolation). The model uses bilinear interpolation in space to estimate the velocity at the tracer location.

We select the tracers' initial positions in the vicinity of a given AR by randomly selecting 2,000 points from the entire study domain ( $-80^\circ\text{S}$  to  $80^\circ\text{N}$ ,  $180^\circ\text{W}$  to  $180^\circ\text{E}$ ), with a probability given by a 2D Gaussian function centered in the AR

$$g(x, y) = \exp(-(a(x - \bar{x})^2 + 2b(x - \bar{x})(y - \bar{y}) + c(y - \bar{y})^2)), \quad (11)$$



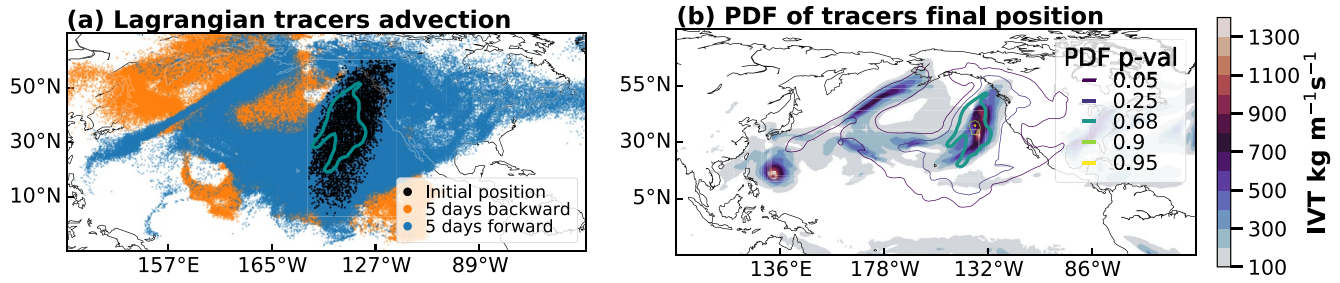


**Figure 5.** (a) Initial position (black), after 5 days backward advection (orange), and 5 days forward advection from the orange tracer locations (blue). The cyan contour shows the region with most (68%) of the tracers after the 5-day forward advection. (b) Integrated vapor transport (filled contours) and probability density function of the tracers' final position (contours). Thicker cyan contour at  $p = 0.68$  area is used to estimate the atmospheric river size in the Lagrangian tracers method (LT).

where

$$a = \frac{\cos^2(\theta)}{2\lambda_0^2} + \frac{\sin^2(\theta)}{2\lambda_1^2}, \quad (12)$$

$$b = \frac{\sin(2\theta)}{4\lambda_0^2} - \frac{\sin(2\theta)}{4\lambda_1^2}, \quad (13)$$

$$c = \frac{\sin^2(\theta)}{2\lambda_0^2} + \frac{\cos^2(\theta)}{2\lambda_1^2}, \quad (14)$$

$\lambda_0$  and  $\lambda_1$  are the eigenvalues of the covariance matrix in Equation 5,  $\bar{x}$  and  $\bar{y}$  are the longitude and latitude of the AR center, and  $\theta$  is the angle between the along the AR axis ( $\bar{s}_1$  from Equation 5) and the equator. We observe that for fewer than 500 tracers, the AR area might not be correctly resolved since, for larger ARs, there might be regions inside the AR without initial tracers. We find that, in general, 2,000 is a sufficient number of initial tracers and allows a spatial distribution that concentrates in the vicinity of the IVT blob and extends further from it. Our results do not vary for larger number of tracers. In this fashion, we ensure that the initial position of tracers is distributed inside and outside of the AR, but no tracers (or a negligible number) are far from the AR (the tracers initial position distribution is represented by the black dots in Figure 5a). Additionally, we simulate 50 tracers for each initial position, resulting in 50 different trajectories due to the random term in Equation 10. This is equivalent to repeating the Experiment 50 times, thus increasing the statistical robustness of the results. We find similar results using a higher number of repetitions.

The area estimation is done as follows. Starting from the initial position (black dots), we compute trace trajectories five days backward in time (resulting in the orange dots in Figure 5a). We then use these new locations to calculate the forward in time 5-day trajectory (resulting in the blue dots in Figure 5a). We compute this process for all pressure levels between the surface and 500 hPa and record the tracers' final position at each level. We choose 5 days because we need a timescale longer than the boundary layer and convective timescales, and we want a timescale as long as possible without exceeding the Rossby timescale by too much. Moreover, other works have found that few ARs have a longer duration than 5 days (Payne & Magnusdottir, 2016; Zhou et al., 2018).

We gather the final tracers from all levels and calculate the bivariate PDF of the final tracer latitudes and longitudes. We estimate the AR area as the size of the largest contiguous contour of PDF = 0.68 (the PDF of the final position within two standard deviations), corresponding to the thicker green contour of Figure 5b. Text S2 and Figure S3 show a sensitivity test of AR area relative to PDF value changes.

### 3.4. ClimateNet Method (CN)

We use *ClimateNet* Climate Contours (<https://www.nersc.gov/research-and-development/data-analytics/big-data-center/climatenet/>, [http://labelmegold.services.nersc.gov/climatecontours\\\_gold/tool.html](http://labelmegold.services.nersc.gov/climatecontours\_gold/tool.html)), which is a guided user interface for annotating climate events, facilitating the collection of hand-labeled weather data sets (Kashinath et al., 2021).

We use the data generated using the ClimateNet labeling tool during the third ARTMIP workshop (<http://www.cgd.ucar.edu/projects/artmip/meetings.html>) in October 2019. Half a day out of a 2.5-day workshop was devoted to this task, including over 15 workshop participants who labeled 660 time slices of data during the session (O'Brien et al., 2020). A total of 1,822 AR detections were made over the whole globe, and 378 were made in the North Pacific Ocean region (which will be referred to as global and NP, respectively) using an Atmospheric Model Intercomparison Project (AMIP) simulation performed with the Community Atmosphere Model (version 5) running at 25-km resolution (Wehner et al., 2014). We calculate the area and orientation of each of these hand-labeled ARs. Unlike the methods described in Sections 3.1–3.3, this method does not distinguish between the AR-genesis location or life cycle.

### 3.5. AR Size Calculation Methods Summary

To help the reader keep track of the various methods used in this study, Table 1 summarizes a description for each method and the short names used throughout this study.

## 4. Results

We focus on the size of North American landfalling ARs. Our results are consistent among methods: with AR areas within the  $10^{11}$ – $10^{12}$  m<sup>2</sup> range in four of the five methods: PC, LT, BG, and SO; and between  $10^{11}$  and  $10^{13}$  m<sup>2</sup> for CN. Our results have a narrower range of AR area than the ARTMIP ensemble (Figure 1), with order-of-magnitude consistency with the majority of the algorithms used in ARTMIP. The novel statistical methods in this study (PC, SO, BG, and LT) are in good agreement with the manually labeled AR sizes from the ClimateNet method. Table 2 contains a summary of the length, width, and area for all four methods, depending on the AR genesis location and life cycle. Figure 8 shows a visual representation of the size results for PC, LT, BG, and SO methods for WP and EP at 50% life cycle.

### 4.1. AR Length and Width

Figures 6a–6c show the PDF of length and width calculated by PC. The PDF exhibits the typical “long and narrow” AR shape, from 2.3 to 4.5 times longer than the width (Table 3). According to PC, ARs have a median width of 844 km (90% of the cases were between 520 and 1,386 km), and length of 3,842 km (90% between 2,495 and 5,816 km) for the AR with WP origin; and median width of 814 km (90% of the cases were between 6,477 and 1,476 km), and length of 3,413 km (90% between 2,321 and 5,400 km) for the ARs with EP Origin.

According to PC, WP has larger and wider ARs than EP. The differences in length are statistically significant at a 99% confidence level, however, differences in width are not. Concerning the life cycle, the WP composite has the smallest AR size at 25% and the largest at 50% of its life cycle, nevertheless, only the differences in length are statistically significant. The EP composite length does not change much through the life cycle. However, the width decreases monotonically through its life cycle, with differences statistically significant at a 99% confidence level.

Consistently with PC, BG, and SO methods show larger ARs originated in the WP. According to BG, the ARs composite length (width) at 50% life cycle is 4,019 (1,121) km for the WP and 3,275 (501) km for the EP. The SO's composite length (width) at 50% life cycle is 2,751 (916) km for the WP and 2,107 (646) km for the EP. It is possible that the EP and WP ARs' size differences might come from the landfall condition and that focusing on landfall means that we are preferentially looking at that type of AR, since this study is focused specifically on landfalling ARs. The difference in size between WP and EP ARs and of non-land-falling ARs could be explored in future study.

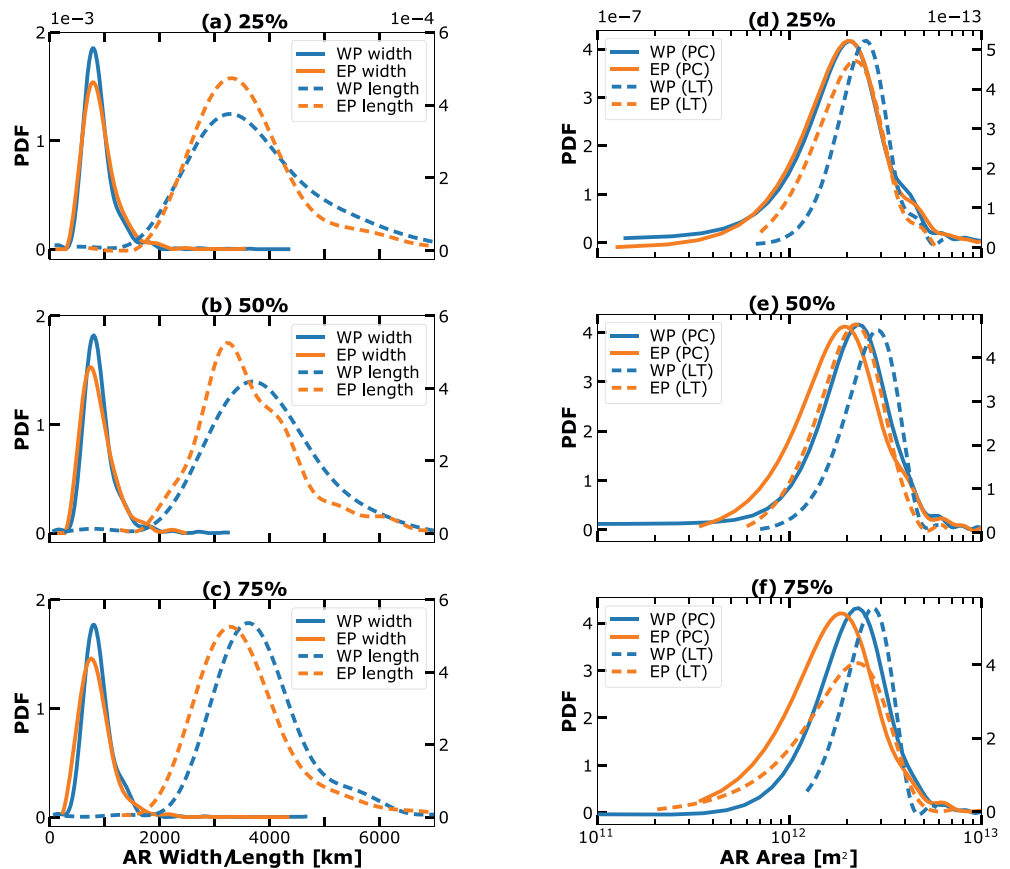


**Figure 6.** (a–c) Probability density function (PDF) of atmospheric river (AR) length (dashed lines) and width (solid lines) using the principal components method (PC), at 25%, 50%, and 75% of the AR life cycle. WP composite in blue lines, EP composite in orange lines. (d–f) PDF of AR area for the PC method in solid lines, and the LT method in dashed lines. Lines colors are the same as in (a–c).

The lengths determined by the BG and SO methods exhibit little variation throughout the life cycle. In contrast, AR width decreased by a factor of 0.67 (WP) and 0.60 (WP) for BG, and 0.85 (WP) 0.69 (EP) for SO. These results suggest that the AR area difference through the life cycle is mainly due to changes in width.

#### 4.2. AR Area

Figures 6d and 6e show the PDFs of the AR area, calculated by PC method (solid lines) and LT (dashed lines). For the WP ARs, the area has a median of  $2.47 \times 10^{12}$  and  $2.75 \times 10^{12}$  m<sup>2</sup> for PC and LT, respectively. For the EP ARs, the area has a median of  $2.23 \times 10^{12}$  and  $2.33 \times 10^{12}$  m<sup>2</sup> for PC and LT, respectively. The WP composite has larger areas than the EP at a 99% confidence level. EP ARs do not show a significant difference in the area through the life cycle, while WP ARs attain maximum area at their mid-life cycle for both the PC and LT methods.

The one-tailed KS-test (one-tailed BG) estimates the AR composite area as  $3.67 \times 10^{12}$  and  $1.40 \times 10^{12}$  m<sup>2</sup> for WP and EP, respectively (at 50% life cycle). SO estimates a composite area of  $1.75 \times 10^{12}$  and  $8.74 \times 10^{11}$  m<sup>2</sup> for WP and EP, respectively (at 50% life cycle), with more extensive (both width and length) AR from WP when compared with the EP AR.

BG results show a decrease in AR composite area through the life cycle by a factor of 0.68 and 0.54 for the WP and EP, respectively (decrease of  $\sim 0.83$  and  $\sim 0.62$  according to SO). These changes come mainly from differences in width.

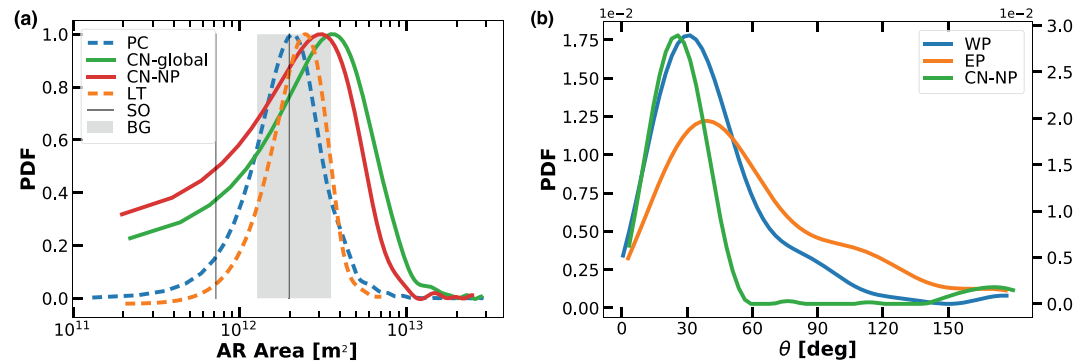


**Figure 7.** (a) Probability density functions (PDFs) of atmospheric river (AR) area (PDFs are not normalized for visualization). PDFs from the PC and LT methods are calculated using data from WP and EP at 50% life cycle. The lowest to highest obtained values from the BG (SO) methods are represented in the shaded gray area (between solid gray lines) for comparison. (b) PDF of AR orientation with respect to the equator from the PC method at 50% of the AR life cycle for the WP (blue line), EP (orange line), and the North Pacific ClimateNet (green line) composites.

CN results show a median area of  $3.34 \times 10^{12} \text{ m}^2$  (90% of data between  $6.15 \times 10^{11}$  and  $7.70 \times 10^{12} \text{ m}^2$ ) in the North Pacific region. Figure 7a shows larger AR areas for the global analysis  $4.29 \times 10^{12} \text{ m}^2$  (90% of data between  $9.43 \times 10^{11}$  and  $1.09 \times 10^{13} \text{ m}^2$ ). All the other methods (PC, LT, BG, and SO) are consistent with the CN area result, which are in fact hand-labeled AR by experts, demonstrating that these methods give reasonable estimates for AR size. If so, our results using ClimateNet might be on the larger side in terms of AR area, which could be related to the specific shapes the user can determine, or where the user exactly locates the AR “boundary” polygon at the time of labeling, however, these details are outside of the scope of this study.

The sensitivity tests (Text S1 and S2 and Figures S1–S3) show that for the SO method, variations in the overlapping background PDF and composite CPD values from (PDF, CPD)=(0.05,0.95) (minimum overlapping) to (PDF, CPD)=(0.5,0.5) (large overlapping) result in area changes from  $2.84 \times 10^{11}$  to  $9.97^{12} \text{ m}^2$ . The one-tailed BG sensitivity test to the significance level ( $p = 0.8$  to  $p = 0.99$ ) shows a change in AR area from  $2.26^{12}$  to  $1.48^{12} \text{ m}^2$ . For BG and SO, AR length shows more sensitivity to variations in the parameters than width.

The LT sensitivity test shows that using 0.68 as the PDF contour to define AR size, variations in the scaling velocity (from 0.125 times to 4 times  $\sqrt{u}$ ) result in an area changes from  $1.53^{12}$  to  $4.16^{12} \text{ m}^2$ . Variations in the PDF value used (ranging from 0.4 to 0.93) result in area changes between one and two orders of magnitude (Text S2 and Figure S2). All the sensitivity analysis described here are computed for the WP at 50% life cycle. We find similar results for different stages of the life cycle and for EP.

### 4.3. AR Orientation

Figure 7b shows the PDF of the AR orientation with respect to the equator  $\theta$ , calculated using PC and CN methods. PC method results show that ARs originating in the WP are more zonally orientated than those originating in the EP. WP ARs have a median  $\theta$  of  $13.7^\circ$  (with 90% of the data between  $7.7^\circ$  and  $99.8^\circ$ ). EP ARs have a median  $\theta$  of  $49.1^\circ$  (with 90% of the data between  $10.4^\circ$  and  $142.6^\circ$ ). CN results show a median  $\theta$  of  $26.5^\circ$  (with 90% of the data between  $6.9^\circ$  and  $157.2^\circ$ ) for the North Pacific AR.

With respect to the AR life cycle, both WP and EP show an increase in the median  $\theta$ :  $28^\circ$ – $37^\circ$  for the WP, and  $46^\circ$ – $53^\circ$  for the EP. Table 2 summarizes the results of length, width, and area of the AR composite from all the methods in this work. AR geometrical characteristics (aspect ratio and orientation) are summarized in Table 3.

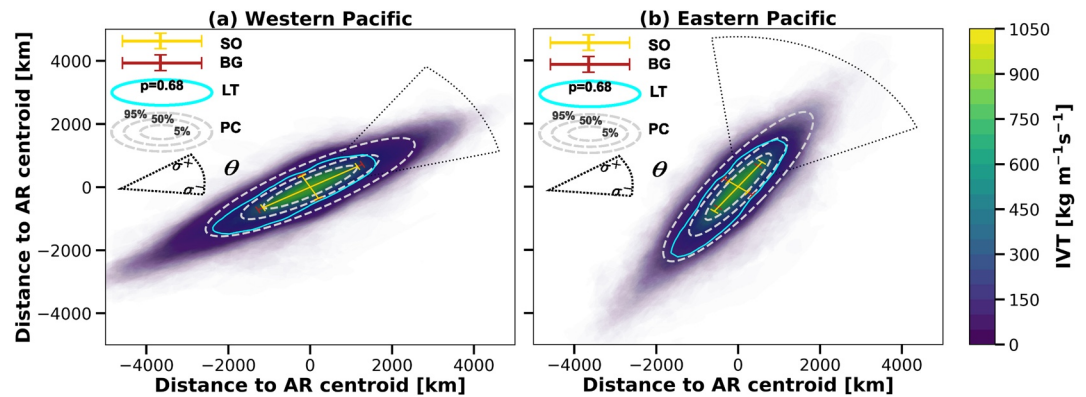


**Figure 8.** Summary of results and graphical comparison for the different size estimation methods. In color contours, we superimpose (with transparency of 0.1%) the integrated vapor transport field of all the atmospheric river (AR) objects available at 50% life cycle for (a) Western Pacific and (b) Eastern Pacific. Each AR object is rotated to the median angle of orientation, and the distance to the center is calculated to make this plot. The dotted “fan” represents two standard deviations for the AR orientation with respect to the equator. The red and gold lines represent the length and width estimated using the SO and BG methods, respectively. Gray dashed lines represent the results of the PC method for the 5th, 50th, and 95th percentile. The cyan solid line represents the results of the LT method. It is the 0.68 probability contour of the final position for all the AR cases gathered and rotated to the same frame of reference.

## 5. Discussion and Conclusions

Figure 8 color contours show the superimposition of IVT from all the AR objects in this study for WP and EP at 50% AR life cycle. We present Figure 8 as a summary of the PC, SO, BG, and LT methods. We aim to illustrate the methods together and make them more clear to the reader. To generate this plot, we rotated all the AR objects to the same frame of reference. The angle of orientation  $\theta$  of each AR represents the median angle with respect to the equator, and the dotted angle is the  $-1$  and  $+1$  standard deviations of  $\theta$ . EP ARs are not only more zonally oriented, but they also have greater variance in  $\theta$  than WP ARs. The break gray lines represent the 5th, 50th, and 95th percentile of the PC method. The golden and red bars represent the SO and BG length and width. The solid cyan line represented the LT method and was created by rotating the final position of tracers to the same system of reference of the plot and then calculating the bivariate PDF (cyan contour corresponds to  $p = 0.68$ ). We can see that BG, SO, PC, and LT are very consistent in estimating the AR width. On the other hand, AR length seems to have more variability among methods (in the supporting information, we show that AR length shows to be more sensitive than width to parameter variations). The results from LT show an asymmetric contour with an elongated tail to the southwest end of the AR. They suggest that an AR detection algorithm based on “fluid dynamics” could be helpful to determine the AR boundaries independently of thresholds or parameter choices and other variables such as IVT. This is worthy of exploring in future works.

**Table 1**  
Methods for AR Size Estimation Used in This Work

Acronym	Description	Section
PC	Principal components analysis of atmospheric river integrated vapor transport field	§3.1
SO	Statistical overlapping of AR composite conditional probability distribution of IVT given the distance to the AR center and the PDF of the background IVT field	§3.2.2
BG	Comparison of the IVT CDF of AR composite with the CDF of the background IVT field	§3.2.3
LT	PDF of Lagrangian tracers final position near an AR after backward and forward 5 days advection	§3.3
CN	Hand-labeled ARs using CLIMANET contours labeling tool by a group of experts at the 2019 ARTMIP workshop	§3.4

**Table 2**  
*Summary of AR Size Statistics by Method*

	Northwest Pacific			Northeast Pacific		
	0.25	0.5	0.75	0.25	0.5	0.75
<b>Method</b>	<b>Length [km]</b>					
<b>PC</b>	3,553	3,842	3,757	3,366	3,413	3,425
5%–95%	2,168–5,984	2,495–5,816	2,608–5,562	2,239–5,596	2,321–5,454	2,315–5,400
<b>BG</b>	2,783	2,932	2,813	2,431	1,640	1,764
<b>SO</b>	2,422	2,650	2,532	1,986	1,944	1,580
<b>Method</b>	<b>Width [km]</b>					
<b>PC</b>	823	844	838	845	814	809
5%–95%	520–1,386	530–1,405	510–1,366	513–1,550	477–1,476	454–1,516
<b>BG</b>	664	912	769	465	882	355
<b>SO</b>	850	812	771	625	582	394
<b>Method</b>	<b>Area [<math>10^{12}</math> m<sup>2</sup>]</b>					
<b>PC</b>	2.32	2.60	2.49	2.26	2.24	2.19
5%–95%	1.02–5.29	1.23–5.22	1.26–4.98	1.03–5.30	1.03–5.09	0.97–5.22
<b>LT</b>	2.55	2.91	2.74	2.35	2.34	2.32
5%–95%	1.52–4.54	1.49–4.47	1.59–3.88	1.26–4.32	1.25–3.97	1.09–4.01
<b>BG</b>	1.45	2.10	1.70	0.88	1.13	0.49
<b>SO</b>	1.61	1.69	1.53	0.97	0.89	0.48
<b>CN</b>	3.34					
5%–95%	0.61–7.70					

In previous studies, two main areas of AR-genesis have been identified: over the subtropical Northwest Pacific and the Northeast Pacific (Sellars et al., 2017; Zhou et al., 2018). Here, we find robust evidence of a statistically significant difference in size of landfalling ARs, depending on their region of genesis, with longer and broader ARs from the Northwest Pacific relative to those originating over the Northeast Pacific. This result may be related to the dynamical process driving the AR formation. It has previously been suggested that WP ARs have a stronger association with a thermally driven jet over the North Pacific Ocean; while EP ARs are thought to be more associated with extratropical cyclone activity and to the commonly known

**Table 3**  
*Summary of AR Geometry Statistics by Method*

	Northwest Pacific			Northeast Pacific		
	0.25	0.5	0.75	0.25	0.5	0.75
<b>Method</b>	<b>Aspect ratio [width/length]</b>					
<b>PC</b>	4.2	4.5	4.4	3.9	4.2	4.3
5%–95%	2.3–7.6	2.3–7.7	2.6–7.3	2.3–7.1	2.3–7.4	2.4–7.5
<b>BG</b>	4.1	3.2	3.6	5.2	1.8	4.9
<b>SO</b>	2.8	3.2	3.2	3.1	3.3	4.0
<b>Method</b>	<b>Orientation [deg.]</b>					
<b>PC</b>	28.9	29.5	35.7	49.9	53.1	53.6
5%–95%	8.1–80.2	7.3–89.2	8.5–111.8	9.5–136.5	12.3–130.1	12.1–149.6
<b>CN</b>	26.5					
5%–95%	6.9–157.2					



phenomenon “Pineapple Express” (Cordeira et al., 2013; Li & Wettstein, 2012; Zhang & Ralph, 2021; Zhang et al., 2019; Zhou & Kim, 2019). We also found evidence WP ARs tend to have more zonal orientation than those originating in the EP, which we believe could also relate to the dynamical feature driving the AR. This difference in AR size and orientation between the EP and WP may have implications for where moisture transport occurs.

PC, BG, and SO methods agree on the typical “long and narrow” shape from the AR literature, with a median aspect ratio of approximately 4 (length/width). Other detection algorithms could use these findings as geometrical constraints in the future. The AR orientation difference between WP and EP could also directly affect the precipitation associated with landfalling AR, depending on the relative angle to the coastal mountain range, and hence the orographic lifting (Hu et al., 2017). More meridionally oriented AR toward the end of the life cycle might modify the effects of orographic lifting and AR impacts over the coast. Furthermore, the steepening of the AR orientation with life cycle supports the hypothesis that most—if not all—ARs are intrinsically related to midlatitude cyclones. During the growth phase of the AR, the AR would form along the southern portion of a midlatitude cyclone, in the location of the dominant moisture source; the predominantly westerly flow would cause developing ARs to have a more zonal orientation. As the AR matures and its moisture is entrained into the cyclone, more of the vapor transport would occur along the eastern flank of the cyclone, giving the AR a steeper, more meridional orientation. If there is a relationship between size, duration, propagation speeds, and orientation, this could influence the AR landfalling conditions and its impacts, which is a question worthy of further investigation.

It is worth noting that the AR width at the end of life cycle (75%) obtained from SO and BG (355 and 394 km, respectively) is in good agreement with airborne and satellite observations from the 1997/1998 winter ARs, where they find an average width scale based in IWV of 417.3 km (Ralph et al., 2004). Moreover, our result on orientation of EP ARs at the end of the life cycle (53.6°) agrees with the 17-case composite observation from dropsondes, where Ralph et al. (2004) find an average wind direction of the low-level jet of 216.7° (corresponding to 53.3° from our methodology’s frame of reference).

We also observe a monotonic decrease in AR width through the life cycle, which could be associated with a systematic loss of moisture, or it could be associated with frontogenesis and sharpening of the frontal zone. These results could be explored in future studies, especially ones using a tracer technique.

The sensitivity tests suggest that for the statistical size estimation methods (SO and BG), length is more sensitive to the choice of parameters than width. We hypothesize that this is related to the difficulty of statistically distinguishing the AR “tail” (or southwest end of AR) from the high water vapor and IVT in the vicinity of the ITCZ. We observe (in a case-by-case exploration) that sometimes the IVT field does not have a clear boundary with respect to the ITCZ, resulting in a noisier CPD in the left side of the AR composite for large probability contours ( $C > 0.9$ ). It is possible that this would also have an impact in the detection and tracking algorithms and their ability to objectively determine the AR boundary.

Furthermore, this raises the question about a possible link between AR size and duration, and how the size of AR might be directly related to hydrological impacts over landfalling regions. Do we need to explicitly include size in addition to IVT intensity and duration in the categorization scale for AR (Ralph et al., 2019) and their impacts? We often assume ergodicity, but if larger ARs have systematically slower/faster propagation speeds, then the AR size-life cycle (and possibly landfalling duration) relationship would not be ergodic. Our future research will study toward answering these questions.

In Figure 1, we can observe a high spread in the size of AR among AR detection methods (white background part). Our results show values with much less spread (colored background part) relative to the current methods. It is important to notice that some of these conclusions could be reached by analysis of existing ARTMIP data, with the caveat that such conclusions would depend on the heuristic AR detection algorithms employed in ARTMIP. The novel analytical contributions introduced in this manuscript—use of PCA of the IVT field, statistical estimation of AR composite size (BG and SO methods), and the use of Lagrangian tracers to determine AR size—allow us to reach these conclusions and can provide a statistical constraint on AR size for other detection methods. This could also allow us to incorporate size into the ARs categorization in coastal regions and their impacts.

**Acknowledgments**

This study was supported by the Director, Office of Science, Office of Biological and Environmental Research of the U.S. Department of Energy Regional and Global Modeling and Analysis (RGMA) and used resources of the National Energy Research Scientific Computing Center (NERSC), also supported by the Office of Science of the U.S. Department of Energy under Contract no. DE-AC02-05CH11231. The authors would like to acknowledge the Research Data Archive (RDA), managed by the Data Engineering and Curation Section (DECS) of the Computational and Information Systems Laboratory (CISL) at the National Center for Atmospheric Research for providing the ERA5 data set at <https://rda.ucar.edu/datasets/ds633.0/>. The authors would like to acknowledge the ClimateNet team who facilitated the labeling tool and data for the ARTMIP workshop AR labeling campaign, in alphabetical order: Karthik Kashinath, Sol Kim, Jiayi Chen, and Kevin Yang. The authors would like to acknowledge participants in the ARTMIP workshop ClimateNet AR labeling campaign, in alphabetical order: Alan Rhoades, Allison Michaelis, Ashley Payne, Brian Kawzenuk, Eric Shearer, Huanping Huang, Jonathan Rutz, Paul Ullrich, Sol Kim, Swen Brands, Yang Zhou, and Zhenhai Zhang. The authors would like to thank the National Council of Science and Technology of Mexico (CONACYT) and UC Mexus for the doctoral fellowship #409048 that partially supported this work. The authors would like to thank the three anonymous reviewers, whose input greatly improved the presentation and quality of this article. This project was supported by the Environmental Resilience Institute, funded by Indiana University's Prepared for Environmental Change Grand Challenge initiative. This manuscript has been authored by an author at Lawrence Berkeley National Laboratory under Contract No. DE-AC02-05CH11231 with the U.S. Department of Energy. The U.S. Government retains, and the publisher, by accepting the article for publication, acknowledges, that the U.S. Government retains a non-exclusive, paid-up, irrevocable, worldwide license to publish or reproduce the published form of this manuscript, or allow others to do so, for U.S. Government purposes.

We speculate that different algorithms within ARTMIP detect different parts of the AR since each algorithm defines different rules and relatively unconstrained thresholds, as it has been shown before by Lora et al. (2020). For example, since algorithms 1–4 are outside the range of areas estimated in this study, we can confidently argue that these algorithms are not detecting the same part of ARs as our methods or as algorithms 11–28. The AR research community may need to define more than one term, with different definitions depending on what particular meteorological feature of AR is being studied. We acknowledge that different algorithms are created with different objectives and study goals in mind. However, future studies could benefit from the definition of three potential new terms: “AR core” (algorithms 1–4), “dynamical envelope” (LT method and maybe 9–17 methods), and “thermodynamic envelope” (PC, BG, SO, CN and algorithms 18–28). Although the dynamical and thermodynamical envelopes are indistinguishable here, they may not be in studies of future AR size. This could help to understand what is the extent of the consistency in AR detection among different algorithms, particularly with respect to size. The importance of changes in AR statistics in the future has been demonstrated before. Previous studies have shown that AR frequency will increase by ~50% globally, AR intensity will increase by ~25%, and that the ARs will be ~25% longer and ~25% wider (Espinoza et al., 2018; Massoud et al., 2019). In future simulations using CMIP5/CMIP6 models, AR detection algorithms project a global increase in AR frequency and sizes, especially along the western coastlines of the Pacific and Atlantic oceans, and it has been demonstrated that the choice of the detection algorithm can have a major impact on the results of the climate change AR studies (O'Brien et al., 2021).

We will continue to examine the relation between AR size and duration. Moreover, the direct relationship we found between AR origin location and size, the life cycle and size, motivates us to apply our methodology to understand how the AR size would change under global warming scenarios. Current detection methods may require adjusting the parameters and thresholds when studying different climate scenarios, making the objective study of change in AR size a challenging problem for future projections. Our approach could provide an objective insight for future works into the possible changes and hydrological impacts due to AR size and climate change.

**Data Availability Statement**

ERA5 data set at <https://rda.ucar.edu/datasets/ds633.0/>.

**References**

Cordeira, J. M., Martin Ralph, F., & Moore, B. J. (2013). The development and evolution of two atmospheric rivers in proximity to western north pacific tropical cyclones in October 2010. *Monthly Weather Review*, 141(12), 4234–4255. <https://doi.org/10.1175/MWR-D-13-00019.1>

Dettinger, M. D. (2011). Climate change, atmospheric rivers, and floods in California – A multimodel analysis of storm frequency and magnitude changes. *Journal of the American Water Resources Association*, 47(3), 514–523. <https://doi.org/10.1111/j.1752-1688.2011.00546.x>

Dettinger, M. D. (2013). Atmospheric rivers as drought busters on the U.S. west coast. *Journal of Hydrometeorology*, 14(6), 1721–1732. <https://doi.org/10.1175/jhm-d-13-02.1>

Dirmeyer, P. A., & Brubaker, K. L. (2007). Characterization of the global hydrologic cycle from a back-trajectory analysis of atmospheric water vapor. *Journal of Hydrometeorology*, 8(1), 20–37. <https://doi.org/10.1175/jhm557.1>

Eldardiry, H., Mahmood, A., Chen, X., Hossain, F., Nijssen, B., & Lettenmaier, D. P. (2019). Atmospheric river-induced precipitation and snowpack during the Western United States Cold Season. *Journal of Hydrometeorology*, 20(4), 613–630. <https://doi.org/10.1175/jhm-d-18-0228.1>

Espinoza, V., Waliser, D. E., Guan, B., Lavers, D. A., & Ralph, F. M. (2018). Global analysis of climate change projection effects on atmospheric rivers. *Geophysical Research Letters*, 45(9), 4299–4308. <https://doi.org/10.1029/2017GL076968>

European Centre for Medium-Range Weather Forecasts. (2019). *ERA5 reanalysis (0.25 degree latitude-longitude grid)*. Research Data Archive at the National Center for Atmospheric Research, Computational and Information Systems Laboratory. <https://doi.org/10.5065/BH6N-5N20>

Garaboa-Paz, D., Eiras-Barca, J., Huhn, F., & Pérez-Muñuzuri, V. (2015). Lagrangian coherent structures along atmospheric rivers. *Chaos: An Interdisciplinary Journal of Nonlinear Science*, 25(6), 063105. <https://doi.org/10.1063/1.4919768>

Gelaro, R., McCarty, W., Suárez, M. J., Todling, R., Molod, A., Takacs, L., et al. (2017). The modern-era retrospective analysis for research and applications, version 2 (MERRA-2). *Journal of Climate*, 30(14), 5419–5454. <https://doi.org/10.1175/JCLI-D-16-0758.1>

Goldenson, N., Leung, L. R., Bitz, C. M., & Blanchard-Wrigglesworth, E. (2018). Influence of atmospheric rivers on mountain snowpack in the western United States. *Journal of Climate*, 31(24), 9921–9940. <https://doi.org/10.1175/JCLI-D-18-0268.1>

Griffa, A., Owens, K., Piterbarg, L., & Rozovskii, B. (1995). Estimates of turbulence parameters from Lagrangian data using a stochastic particle model. *Journal of Marine Research*, 53(3), 371–401. <https://doi.org/10.1357/0022240953213151>

Guan, B., Molotch, N. P., Waliser, D. E., Fetzer, E. J., & Neiman, P. J. (2010). Extreme snowfall events linked to atmospheric rivers and surface air temperature via satellite measurements. *Geophysical Research Letters*, 37(20). <https://doi.org/10.1029/2010GL044696>

- Hu, H., Dominguez, F., Wang, Z., Lavers, D. A., Zhang, G., & Ralph, F. M. (2017). Linking atmospheric river hydrological impacts on the U.S. west coast to Rossby wave breaking. *Journal of Climate*, 30(9), 3381–3399. <https://doi.org/10.1175/JCLI-D-16-0386.1>
- Kashinath, K., Mudigonda, M., Kim, S., Kapp-Schwoerer, L., Graubner, A., Karaismailoglu, E., et al. (2021). ClimateNet: An expert-labelled open dataset and deep learning architecture for enabling high-precision analyses of extreme weather. *Geoscientific Model Development Discussions*, 14(1), 107–124. <https://doi.org/10.5194/gmd-2020-72>
- Kim, J., Waliser, D. E., Neiman, P. J., Guan, B., Ryoo, J. M., & Wick, G. A. (2013). Effects of atmospheric river landfalls on the cold season precipitation in California. *Climate Dynamics*, 40(1–2), 465–474. <https://doi.org/10.1007/s00382-012-1322-3>
- LaCasce, J. (2008). Statistics from Lagrangian observations. *Progress in Oceanography*, 77(1), 1–29. <https://doi.org/10.1016/j.pocean.2008.02.002>
- Lavers, D. A., & Villarini, G. (2013a). Atmospheric rivers and flooding over the central United States. *Journal of Climate*, 26(20), 7829–7836. <https://doi.org/10.1175/JCLI-D-13-00212.1>
- Lavers, D. A., & Villarini, G. (2013b). The nexus between atmospheric rivers and extreme precipitation across Europe. *Geophysical Research Letters*, 40(12), 3259–3264. <https://doi.org/10.1002/grl.50636>
- Li, C., & Wettstein, J. J. (2012). Thermally driven and eddy-driven jet variability in reanalysis. *Journal of Climate*, 25(5), 1587–1596. <https://doi.org/10.1175/JCLI-D-11-00145.1>
- Lora, J. M., Mitchell, J. L., Risi, C., & Tripathi, A. E. (2017). North Pacific atmospheric rivers and their influence on western North America at the Last Glacial Maximum. *Geophysical Research Letters*, 44(2), 1051–1059. <https://doi.org/10.1002/2016gl071541>
- Lora, J. M., Shields, C. A., & Rutz, J. J. (2020). Consensus and disagreement in atmospheric river detection: ARTMIP global catalogues. *Geophysical Research Letters*, 47(20), e2020GL089302. <https://doi.org/10.1029/2020GL089302>
- Massoud, E., Espinoza, V., Guan, B., & Waliser, D. (2019). Global climate model ensemble approaches for future projections of atmospheric rivers. *Earth's Future*, 7(10), 1136–1151. <https://doi.org/10.1029/2019ef001249>
- Mundhenk, B. D., Barnes, E. A., & Maloney, E. D. (2016). All-season climatology and variability of atmospheric river frequencies over the North Pacific. *Journal of Climate*, 29(13), 4885–4903. <https://doi.org/10.1175/JCLI-D-15-0655.1>
- Neiman, P. J., Ralph, F. M., Wick, G. A., Lundquist, J. D., & Dettinger, M. D. (2008). Meteorological characteristics and overland precipitation impacts of atmospheric rivers affecting the west coast of North America based on eight years of SSM/I satellite observations. *Journal of Hydrometeorology*, 9(1), 22–47. <https://doi.org/10.1175/2007jhm855.1>
- Newell, R. E., Newell, N. E., Zhu, Y., & Scott, C. (1992). Tropospheric rivers? – A pilot study. *Geophysical Research Letters*, 19(24), 2401–2404. <https://doi.org/10.1029/92gl02916>
- O'Brien, T. A., Collins, W. D., Rauscher, S. A., & Ringler, T. D. (2014). Reducing the computational cost of the ECF using a nuFFT: A fast and objective probability density estimation method. *Computational Statistics and Data Analysis*, 79, 222–234. <https://doi.org/10.1016/j.csda.2014.06.002>
- O'Brien, T. A., Kashinath, K., Cavanaugh, N. R., Collins, W. D., & O'Brien, J. P. (2016). A fast and objective multidimensional kernel density estimation method: FastKDE. *Computational Statistics & Data Analysis*, 101, 148–160. <https://doi.org/10.1016/j.csda.2016.02.014>
- O'Brien, T. A., Payne, A. E., Shields, C. A., Rutz, J., Brands, S., Castellano, C., et al. (2020). Detection uncertainty matters for understanding atmospheric rivers. *Bulletin of the American Meteorological Society*, 101, 790–E796. <https://doi.org/10.1175/bams-d-19-0348.1>
- O'Brien, T. A., Risser, M. D., Loring, B., Elbashandy, A. A., Krishnan, H., Johnson, J., & Collins, W. D. (2020). Detection of atmospheric rivers with inline uncertainty quantification: TECA-BARD v1.0.1. *Geoscientific Model Development*, 13(12), 6131–6148. <https://doi.org/10.5194/gmd-13-6131-2020>
- O'Brien, T. A., Wehner, M. F., Payne, A. E., Shields, C. A., Rutz, J. J., Leung, L. R., et al. (2021). Increases in future AR count and size: Overview of the ARTMIP Tier 2 CMIP5/6 experiment. *Geophysical Research Letters*. <https://doi.org/10.1002/essoar.10504170.1>
- Payne, A. E., & Magnusdottir, G. (2016). Persistent landfalling atmospheric rivers over the west coast of North America. *Journal of Geophysical Research*, 121(22), 13287–13300. <https://doi.org/10.1002/2016JD025549>
- Price, G. R. (1972). Extension of covariance selection mathematics. *Annals of Human Genetics*, 35(4), 485–490. <https://doi.org/10.1111/j.1469-1809.1957.tb01874.x>
- Ralph, F. M., & Dettinger, M. D. (2011). Storms, floods, and the science of atmospheric rivers. *Eos, Transactions American Geophysical Union*, 92(32), 265–266. <https://doi.org/10.1029/2011eo320001>
- Ralph, F. M., Dettinger, M. D., Cairns, M. M., Galarneau, T. J., & Eylander, J. (2018). Defining “atmospheric river”: How the glossary of meteorology helped resolve a debate. *Bulletin of the American Meteorological Society*, 99(4), 837–839. <https://doi.org/10.1175/BAMS-D-17-0157.1>
- Ralph, F. M., Neiman, P. J., & Wick, G. A. (2004). Satellite and CALJET aircraft observations of atmospheric rivers over the Eastern North Pacific Ocean during the winter of 1997/98. *Monthly Weather Review*, 132(7), 1721–1745. [https://doi.org/10.1175/1520-0493\(2004\)132<textless>1721:SACAOO<textgreater>2.0.CO;2](https://doi.org/10.1175/1520-0493(2004)132<textless>1721:SACAOO<textgreater>2.0.CO;2)
- Ralph, F. M., Neiman, P. J., Wick, G. A., Gutman, S. I., Dettinger, M. D., Cayan, D. R., & White, A. B. (2006). Flooding on California's Russian River: Role of atmospheric rivers. *Geophysical Research Letters*, 33(13), 3–7. <https://doi.org/10.1029/2006GL026689>
- Ralph, F. M., Rutz, J. J., Cordeira, J. M., Dettinger, M., Anderson, M., Reynolds, D., et al. (2019). A scale to characterize the strength and impacts of atmospheric rivers. *Bulletin of the American Meteorological Society*, 100(2), 269–289. <https://doi.org/10.1175/BAMS-D-18-0023.1>
- Ramos, A. M., Trigo, R. M., Liberato, M. L. R., & Tomé, R. (2015). Daily precipitation extreme events in the Iberian Peninsula and its association with atmospheric rivers. *Journal of Hydrometeorology*, 16(2), 579–597. <https://doi.org/10.1175/jhm-d-14-0103.1>
- Rodean, H. C. (1996). Stochastic Lagrangian models of turbulent diffusion. *Meteorological Monographs*, 48, 1–84. <https://doi.org/10.1175/0065-9401-26.48.1>
- Rutz, J. J., Shields, C. A., Lora, J. M., Payne, A. E., Guan, B., Ullrich, P., et al. (2019). The atmospheric river tracking method intercomparison project (ARTMIP): Quantifying uncertainties in atmospheric river climatology. *Journal of Geophysical Research: Atmospheres*, 124(24), 13777–13802. <https://doi.org/10.1029/2019jd030936>
- Sawford, B. L. (1991). Reynolds number effects in Lagrangian stochastic models of turbulent dispersion. *Physics of Fluids A: Fluid Dynamics*, 3(6), 1577–1586. <https://doi.org/10.1063/1.857937>
- Sellars, S. L., Kawzenuk, B., Nguyen, P., Ralph, F. M., & Sorooshian, S. (2017). Genesis, pathways, and terminations of intense global water vapor transport in association with large-scale climate patterns. *Geophysical Research Letters*, 44(24), 12465–12475. <https://doi.org/10.1002/2017GL075495>
- Shields, C. A., Rutz, J. J., Leung, L. Y., Martin Ralph, F., Wehner, M., Kawzenuk, B., et al. (2018). Atmospheric River Tracking Method Intercomparison Project (ARTMIP): Project goals and experimental design. *Geoscientific Model Development*, 11(6), 2455–2474. <https://doi.org/10.5194/gmd-11-2455-2018>

- Viale, M., Valenzuela, R., Garreaud, R. D., & Ralph, F. M. (2018). Impacts of atmospheric rivers on precipitation in southern South America. *Journal of Hydrometeorology*, *19*(10), 1671–1687. <https://doi.org/10.1175/jhm-d-18-0006.1>
- Waliser, D., & Guan, B. (2017). Extreme winds and precipitation during landfall of atmospheric rivers. *Nature Geoscience*, *10*(3), 179–183. <https://doi.org/10.1038/ngeo2894>
- Wehner, M. F., Reed, K. A., Li, F., Prabhat Bacmeister, J., Chen, C.-T., Jablonowski, C., et al. (2014). The effect of horizontal resolution on simulation quality in the community atmospheric model, CAM5.1. *Journal of Advances in Modeling Earth Systems*, *6*(4), 980–997. <https://doi.org/10.1002/2013ms000276>
- Zhang, Z., & Ralph, F. M. (2021). The influence of antecedent atmospheric river conditions on extratropical cyclogenesis. *Monthly Weather Review*, *149*(5), 1337–1357. <https://doi.org/10.1175/mwr-d-20-0212.1>
- Zhang, Z., Ralph, F. M., & Zheng, M. (2019). The relationship between extratropical cyclone strength and atmospheric river intensity and position. *Geophysical Research Letters*, *46*(3), 1814–1823. <https://doi.org/10.1029/2018gl079071>
- Zhou, Y., & Kim, H. (2019). Impact of distinct origin locations on the life cycles of landfalling atmospheric rivers over the U.S. west coast. *Journal of Geophysical Research: Atmospheres*, *124*(22), 11897–11909. <https://doi.org/10.1029/2019jd031218>
- Zhou, Y., Kim, H., & Guan, B. (2018). Life cycle of atmospheric rivers: Identification and climatological characteristics. *Journal of Geophysical Research: Atmospheres*, *123*(22), 12715–12725. <https://doi.org/10.1029/2018jd029180>
- Zhu, Y., & Newell, R. E. (1998). A proposed algorithm for moisture fluxes from atmospheric rivers. *Monthly Weather Review*, *126*(3), 725–735. [https://doi.org/10.1175/1520-0493\(1998\)126<0725:apafmf>2.0.co;2](https://doi.org/10.1175/1520-0493(1998)126<0725:apafmf>2.0.co;2)